Faraday Discussions

Cite this: *Faraday Discuss.*, 2017, **201**, 351

PAPER

Ethylene oligomerization in metal–organic frameworks bearing nickel(II) 2,2′-bipyridine complexes†

Miguel I. Gonzalez,[a] Julia Oktawiec[a] and Jeffrey R. Long *[abc]

Received 10th February 2017, Accepted 16th February 2017
DOI: 10.1039/c7fd00061h

The metal–organic frameworks $Zr_6O_4(OH)_4(bpydc)_6$ (**1**; $bpydc^{2-}$ = 2,2′-bipyridine-5,5′-dicarboxylate) and $Zr_6O_4(OH)_4(bpydc)_{0.84}(bpdc)_{5.16}$ (**2**; $bpdc^{2-}$ = biphenyl-4,4′-dicarboxylate) were readily metalated with $Ni(DME)Br_2$ (DME = dimethoxyethane) to produce the corresponding metalated frameworks **1**$(NiBr_2)_6$ and **2**$(NiBr_2)_{0.84}$. Both nickel(II)-containing frameworks catalyze the oligomerization of ethylene in the presence of Et_2AlCl. In these systems, the pore environment around the active nickel sites significantly influences their selectivity for formation of oligomers over polymer. Specifically, the single-crystal structure of **1**$(NiBr_2)_{5.64}$ reveals that surrounding metal–linker complexes enforce a steric environment on each nickel site that causes polymer formation to become favorable. Minimizing this steric congestion by isolating the nickel(II) bipyridine complexes in the mixed-linker framework **2**$(NiBr_2)_{0.84}$ markedly improves both the catalytic activity and selectivity for oligomers. Furthermore, both frameworks give product mixtures that are enriched in shorter olefins (C_{4-10}), leading to deviations from the expected Schulz–Flory distribution of oligomers. Although these deviations indicate possible pore confinement effects on selectivity, control experiments using the nickel-treated biphenyl framework $Zr_6O_4(OH)_4(bpdc)_6(NiBr_2)_{0.14}$ (**3**$(NiBr_2)_{0.14}$) reveal that they likely arise at least in part from the presence of nickel species that are not ligated by bipyridine within **1**$(NiBr_2)_{5.64}$ and **2**$(NiBr_2)_{0.84}$.

Introduction

Heterogeneous catalysts maintain a dominant role in industrial synthesis, accounting for approximately 80% of all catalytic processes.[1] This preference for

[a]*Department of Chemistry, University of California, Berkeley, California, 94720-1462, USA. E-mail: jrlong@berkeley.edu*

[b]*Department of Chemical and Biomolecular Engineering, University of California, Berkeley, California, 94720-1462, USA*

[c]*Materials Sciences Division, Lawrence Berkeley National Laboratory, Berkeley, California, 94720, USA*

† Electronic supplementary information (ESI) available: Single-crystal and powder X-ray diffraction data, adsorption isotherms, thermogravimetric analyses, ethylene oligomerization data, SEM images, supplementary experimental methods. CCDC 1530874. For ESI and crystallographic data in CIF or other electronic format see DOI: 10.1039/c7fd00061h

solid catalysts arises from their greater stability and ease of recovery, which enable higher throughput and lower costs of catalyst separation and replacement. Several key industrial transformations, however, still rely on molecular catalysts to achieve requisite reactivity or selectivity.[2,3] Among these processes, the oligomerization of ethylene to linear α-olefins stands as one of the largest-scale homogeneously-catalyzed reactions, with over 4 million tons of linear α-olefins produced each year as essential precursors to a wide variety of industrial products.[4] Short linear α-olefins (C_4–C_8) are used as comonomers in the industrial synthesis of linear low-density polyethylene. These products are obtained through the highly-selective oligomerization of ethylene to 1-butene (the IFP/Sabic AlphaButol process), 1-hexene (the Chevron-Phillips trimerization process), or 1-octene (the Sasol tetramerization process). On the other hand, higher molecular weight oligomers remain important intermediates in the production of plasticizers (C_6–C_{10}), lubricants (C_{10}–C_{12}), and detergents (C_{12}–C_{16}),[4–6] and are derived from less selective ethylene oligomerization in processes such as the Shell Higher Olefin Process (SHOP). With the intention of providing more practical, economical, and sustainable alternatives to these processes, considerable work has been directed toward developing heterogeneous oligomerization catalysts by immobilization of molecular catalysts on solid supports or ion-exchange in porous inorganic materials.[7–10] Despite these efforts, conventional heterogeneous systems have yet to match both the selectivity and activity of the best molecular catalysts,[11–17] highlighting the need for new materials in developing heterogeneous ethylene oligomerization catalysts.

Metal–organic frameworks, a class of porous crystalline materials, have proven to be exceptionally suited to the design of catalysts that bridge the gap between conventional heterogeneous and homogeneous catalysis. The high crystallinity, well-defined structure, and synthetic diversity of these materials enables control over active sites with a precision approaching that of molecular catalysts.[18–22] Furthermore, isolation of these sites within a porous rigid framework can impart stability to reactive species while maintaining their accessibility to substrates.[23–26] Taking advantage of these attributes, several metal–organic frameworks demonstrate promising activity for ethylene oligomerization,[25–32] with most reports focusing on the selective formation of 1-butene.[26–29,32] Notably, one of these materials, nickel(II)-exchanged $Zn_5Cl_4(btdd)_3$ (H_2btdd = bis(1H-1,2,3-triazolo[4,5-*b*],[4′,5′-i])dibenzo[1,4]dioxin) or Ni-MFU-4l, has been shown to achieve the highest activity for ethylene dimerization for a heterogeneous catalyst, with a selectivity for 1-butene that exceeds that of its molecular analog.[26]

Similar to analogous homogeneous catalysts, the active sites in these frameworks are generally thought to operate through the Cossee–Arlman mechanism (Scheme 1).[27,33,34] Here, chain growth involves successive ethylene insertion into a metal–alkyl intermediate, and chain termination occurs through β-H elimination of the alkyl chain followed by substitution of the resulting olefin by ethylene. The relative rates of chain termination and chain growth govern product selectivity in these systems; catalysts with rates of chain termination that exceed the rate of chain growth selectively form butene, while those with comparable rates of chain termination and growth produce a Schulz–Flory chain length distribution of oligomers. The latter is characterized by an

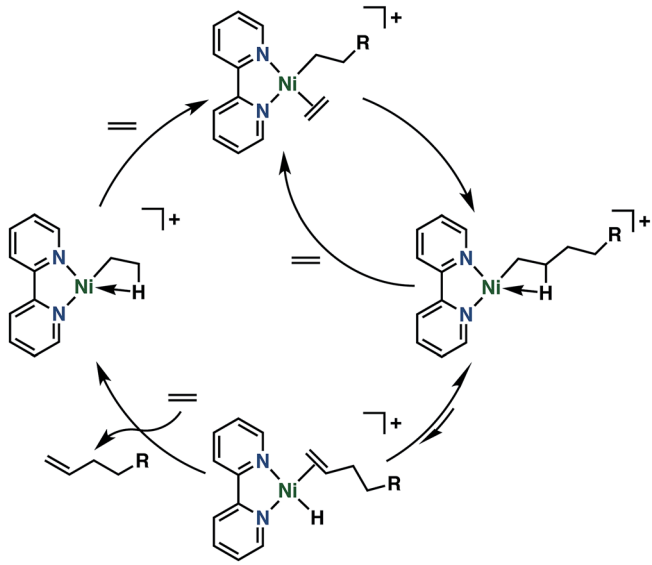

Scheme 1 Cossee–Arlman mechanism for ethylene oligomerization or polymerization catalyzed by nickel(II) bipyridine or α-diimine complexes.

exponential decay in the mole fraction of each oligomer with increasing chain length.[33,35]

Given the continued industrial relevance of C_4–C_{10} α-olefins, we sought to develop new heterogeneous catalysts for the production of higher molecular weight olefins by designing metal–organic frameworks with active sites that give a Schulz–Flory distribution of oligomers. Moreover, because these systems produce intermediates of increasing chain length, the framework pore environment could potentially be used to influence the product selectivity. This influence offers an additional level of structural control over reactivity and has in fact been demonstrated to be a distinct advantage of metal–organic frameworks over molecular systems.[36,37] Conceivably, the metal–alkyl intermediates in these frameworks can grow sufficiently long for confinement within the pore to disfavor further ethylene insertion, resulting in selectivity for shorter oligomers. This selectivity would manifest as deviations from the expected Schulz–Flory product distribution, providing a convenient probe for confinement effects imparted by enclosing the active sites within a rigid framework.

The post-synthetic metalation of metal–organic frameworks has been extensively employed as a versatile strategy for engineering catalytic active sites within these materials.[18–22,24,38–40] Drawing upon the extensive work on ethylene oligomerization using molecular nickel(II) α-diimine and bipyridine complexes,[34,35,41,42] we envisioned that similar nickel(II) complexes could be installed into the 2,2′-bipyridine sites of the previously reported metal–organic framework $Zr_6O_4(OH)_4(bpydc)_6$ (**1**).[18,19,22,43] As functionalized and expanded variants of the thermally and chemically stable framework $Zr_6O_4(OH)_4(bdc)_6$ or UiO-66,[44] **1** and its metalated derivatives have been evaluated for applications in gas separation

and catalysis.[18,19,21,22,45] The three-dimensional pore network of this framework should also accommodate diffusion of both reactants and products, while its ~13 Å-wide octahedral cages should be sufficiently small to induce confinement effects on oligomerization. In addition, the ability to characterize the metal complexes formed in this framework by single-crystal X-ray diffraction provides an invaluable handle in correlating structure to observed reactivity.[18]

Herein, we show that metalation of **1** with Ni(DME)Br_2 yields **1**$(NiBr_2)_6$, which catalyzes the formation of a mixture of oligomers and polymer from ethylene with Et_2AlCl as an activating agent. Characterization of this framework by single-crystal X-ray diffraction (Fig. 1) suggests that steric crowding of the nickel(II)–linker complexes causes these sites to favor production of polyethylene over ethylene oligomers. Both catalytic activity and selectivity can be appreciably enhanced through dispersion of the nickel active sites in the mixed-linker framework **2**$(NiBr_2)_{0.84}$. Finally, the oligomer mixtures produced by these frameworks show deviations from the expected Schulz–Flory distribution, which may be an indication of confinement effects in these reactions. Control experiments reveal, however, that these deviations are at least partially due to the presence of adventitious nickel species.

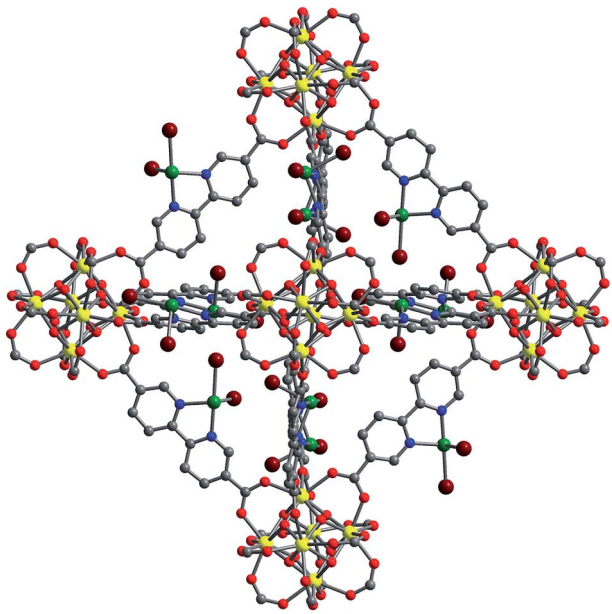

Fig. 1 A portion of the crystal structure of $Zr_6O_4(OH)_4(bpydc)_6(NiBr_2)_{5.64}$ at 100 K as determined by analysis of single-crystal X-ray diffraction data; yellow, green, dark red, red, blue, and gray spheres represent Zr, Ni, Br, O, N, and C atoms, respectively. The Ni^{II} centers are disordered over two positions (Fig. S1†), but are represented here in only one orientation. Coordinated solvent molecules that complete the Ni^{II} coordination sphere could not be modeled due to disorder and weak scattering compared to the Br^- ligands. Hydrogen atoms are omitted for clarity.

Experimental

Materials and methods

All manipulations were performed under an N_2 atmosphere in a VAC Atmospheres glovebox or using standard Schlenk techniques. Cyclohexane was deoxygenated by purging with argon for 1 h and dried using a commercial solvent purification system designed by JC Meyer Solvent Systems. The solvents 1,2-dimethoxyethane (DME) and 1-methoxy-2-(2-methoxyethoxy)ethane (diglyme) were purchased from Sigma-Aldrich, dried over Na/benzophenone (for DME) or 4A molecular sieves (for diglyme), and degassed *via* three successive freeze–pump–thaw cycles. The compound 2,2′-bipyridine-5,5′-dicarboxylic acid (H_2bpydc) was synthesized using a previously published procedure.[46] The compounds $ZrCl_4$ and Ni(DME)Br_2 were purchased from Sigma-Aldrich and used as received. The compound biphenyl-4,4′-dicarboxylic acid (H_2bpdc) was purchased from TCI and used as received. Analytical standards for undecane, 1-butene, 1-decene, 1-dodecene, 1-tetradecene, 1-hexadecene, and 1-octadecene were purchased from Sigma-Aldrich and used as received. Analytical standards for 1-hexene and 1-octene were purchased from TCI and used as received. All other chemicals were purchased from commercial vendors and used as received unless otherwise noted.

Thermogravimetric analyses were carried out with a TA Instruments TGA Q5000 operating at a ramp rate of 1 °C min^{-1} under a 25 mL min^{-1} N_2 flow. All samples were prepared as a slurry in hexanes to minimize exposure to oxygen and moisture during loading into the furnace. Samples were then heated to 100 °C at a rate of 1 °C min^{-1} and held at that temperature for 1 h to evaporate the hexanes prior to analysis. Scanning electron microscopy (SEM) samples were prepared by dispersing crystals in dichloromethane and drop casting onto a silicon chip. In order to dissipate charge, the samples were sputter coated with ~3 nm of Au (Denton Vacuum, LLC). Crystals were imaged at 5 keV/12 μA by field emission SEM (JEOL FSM6430). NMR spectra were acquired on Bruker AVB-400 or AVQ-400 instruments at the University of California, Berkeley NMR facility. All chemical shifts are given in relation to residual solvent peaks or tetramethylsilane. Gas chromatographic analysis was performed using an SRI Instruments 8610V GC equipped with an MXT-1 capillary column (60 m long; 0.53 mm internal diameter; 5.0 μm film thickness) and a Cobra autosampler.

$Zr_6O_4(OH)_4$(bpydc)$_6$ (1). This material was synthesized as a microcrystalline powder using a slight modification to a previously published procedure.[18] Briefly, H_2bpydc (6.11 g, 25.0 mmol), benzoic acid (224 g, 2.00 mol), and *N*,*N*-dimethylformamide (DMF; 1.00 L) from a newly opened bottle were placed into a three-neck 2 L round bottom flask equipped with a Schlenk adapter, glass stoppers, and a magnetic stir bar. The resulting mixture was purged with dry N_2 for 30 min. Solid $ZrCl_4$ (5.83 g, 25.0 mmol) was then added and the mixture was purged with dry N_2 for an additional 30 min. Deionized water (820 μL, 45.5 mmol) was then added and the mixture was heated with magnetic stirring for 5 days at 120 °C under an N_2 atmosphere. After allowing the mixture to cool to room temperature, the solvent was decanted and the resulting white microcrystalline powder was washed by soaking three times in 1 L aliquots of fresh DMF for 24 h at 120 °C, followed by solvent exchange with tetrahydrofuran (THF) *via* Soxhlet extraction

for 3 days. The THF-solvated powder was filtered under dry N_2, followed by heating at 120 °C under dynamic vacuum for 24 h to give fully desolvated $Zr_6O_4(OH)_4(bpydc)_6$. Langmuir surface area: 2743 ± 2 $m^2\ g^{-1}$.

Single crystals of **1** were synthesized following a previously reported procedure.[18] Characterization of the crystals was performed by single-crystal X-ray diffraction.

$Zr_6O_4(OH)_4(bpydc)_{0.84}(bpdc)_{5.16}$ (2). This material was synthesized as a microcrystalline powder by substituting H_2bpydc with a mixture composed of a 1 : 9 molar ratio of H_2bpydc and H_2bpdc in the synthetic procedure for **1** above. The precise linker composition was determined to be 14% $bpydc^{2-}$ and 86% $bpdc^{2-}$ by ^{1}H NMR analysis of a sample digested in a solution of 10 μL HF in 2 mL of DMSO-d_6. Langmuir surface area: 2634 ± 2 $m^2\ g^{-1}$. BET surface area: 2430 ± 20 $m^2\ g^{-1}$.

$Zr_6O_4(OH)_4(bpdc)_6$ (3). This material was taken from the same batch of sample synthesized for a previous report.[18]

General procedure for metalation with Ni(DME)Br_2. Microcrystalline **1** or **2** (50–500 mg), Ni(DME)Br_2 (1.0 equivalent per $bpydc^{2-}$), and DME (7.5 mL) were mixed in a 20 mL Teflon-capped vial. The resulting mixture was then heated for one week on a hot plate at 80 °C to afford a pale yellow powder. After cooling to room temperature, the supernatant solution was decanted and the powder was soaked three times in 15 mL fresh DME for 24 h at 80 °C to remove any unreacted metal source. The solvent was then removed under reduced pressure at 80 °C to give the corresponding metalated framework. Due to an observed reduction in the stability of the framework to moisture upon metalation, the metalation and subsequent manipulations were carried out under an inert atmosphere.

Single crystals of **1** suspended in diglyme were transferred into a 4 mL Teflon-capped vial. Most of the solvent was decanted, followed by addition of microcrystalline **1** (10 mg), Ni(DME)Br_2 (1.0 equivalent per $bpydc^{2-}$ in microcrystalline **1**) and diglyme. The mixture was allowed to react for 1 month at 120 °C, resulting in a color change of both the crystals and the powder to pale yellow. Most of the solution was removed by pipette and the crystals were subsequently soaked three times in 3 mL of fresh diglyme at 120 °C for 24 h, after which they were used for single-crystal X-ray diffraction experiments.

Single-crystal X-ray diffraction. X-ray diffraction analysis was performed on a single crystal of **1**$(NiBr_2)_{5.64}$ coated with Paratone-N oil and mounted on a MiTeGen loop. The crystal was frozen at a temperature of 100 K by an Oxford Cryosystems Cryostream 700 Plus. Data were collected at Beamline 11.3.1 at the Advanced Light Source at Lawrence Berkeley National Laboratory using synchrotron radiation ($\lambda = 0.8856$ Å) on a Bruker D8 diffractometer equipped with a Bruker PHOTON100 CMOS detector. Raw data were integrated and corrected for Lorentz and polarization effects using Bruker AXS SAINT software.[47] Absorption corrections were applied using SADABS.[48] Initial evaluation of the diffraction data suggested that metalation induced a change of space group from $Fm\bar{3}m$ to $P2_13$. Attempts to solve and refine the structure in $P2_13$, however, resulted in unsatisfactory refinement. Solution and refinement in the space group $Pa\bar{3}$ was instead attempted based on previous work describing the change in space group of **1** upon metalation. In the end, this space group gave the most satisfactory refinement. The structure was solved using direct methods with SHELXS[49,50] and refined using SHELXL[51] operated in the OLEX2 (ref. 52) interface. No significant crystal

decay was observed during data collection. Thermal parameters were refined anisotropically for all non-hydrogen atoms. Hydrogen atoms were placed in ideal positions and refined using a riding model for all structures. Moving from $Fm\bar{3}m$ to $Pa\bar{3}$ results in two twin domains related by the lost mirror symmetry. Consequently, a twin law (TWIN 0 1 0 1 0 0 0 0 1 2; BASF = 0.500(2)) was required for the structural refinement. The oxygen atoms of the oxo and hydroxo groups on the zirconium clusters in the structure were disordered, so their site occupancy factors were fixed to give a chemical occupancy of 50%. Hydrogen atoms on the hydroxo groups could neither be found nor placed and were omitted from the refinement but not from the formula. Disorder of the linker–$NiBr_2$ complexes required the use of geometric and displacement parameter restraints. Extensive solvent disorder was found in the pores for $\mathbf{1}(NiBr_2)_{5.64}$ and could not be modeled. Consequently, the unassigned electron density was accounted for using SQUEEZE[53] as implemented in the PLATON[54] interface. Refinement before SQUEEZE was applied gave an R1 of 10.10% (w$R2$ = 32.24%), while applying SQUEEZE resulted in an R1 of 6.51% (w$R2$ = 20.46%).

Powder X-ray diffraction. Diffraction data were collected with 0.02° steps using a Bruker AXS D8 Advance diffractometer equipped with Ni-filtered Cu-Kα radiation (λ = 1.5418 Å), a Göbel mirror, a Lynxeye linear position-sensitive director, and mounting the following optics: a fixed divergence slit (0.6 mm), a receiving slit (3 mm), and a secondary beam Soller slit (2.5°). The generator was set at 40 kV and 40 mA. Samples were either directly loaded on zero background sample holders or packed into capillaries in a nitrogen-filled glovebox and flame-sealed before data was collected by means of scans in the 2θ range of 2–50°. For $\mathbf{1}(NiBr_2)_6$, $\mathbf{2}(NiBr_2)_{0.84}$, and $\mathbf{3}(NiBr_2)_{0.14}$, a standard peak search, followed by indexing through the single value decomposition approach,[55] as implemented in TOPAS-Academic,[56] allowed the determination of approximate unit cell parameters. Analysis of $\mathbf{1}(NiBr_2)_6$ led to the assignment of the space group $Pa\bar{3}$ on the basis of systematic absences. The unit cell and space group were verified by a structureless Pawley refinement. Likewise, samples $\mathbf{2}(NiBr_2)_{0.84}$ and $\mathbf{3}(NiBr_2)_{0.13}$ were also examined, and the space group of the frameworks were found to have remained as $Fm\bar{3}m$.

Low-pressure gas adsorption measurements. Gas adsorption isotherms for pressures in the range 0–1.2 bar were measured by a volumetric method using a Micromeritics ASAP2420 instrument. A typical sample, consisting of ~100 mg of material, was transferred to a pre-weighed analysis tube, which was capped with a Micromeritics TranSeal and evacuated by heating at either 120 °C (**1** and **2**) or 80 °C ($\mathbf{1}(NiBr_2)_6$, $\mathbf{2}(NiBr_2)_{0.84}$, and $\mathbf{3}(NiBr_2)_{0.14}$) at a ramp rate of 1 °C min^{-1} under dynamic vacuum until an outgas rate of less than 3 μbar min^{-1} was achieved. The evacuated analysis tube containing the degassed sample was then carefully transferred to an electronic balance and weighed again to determine the mass of the sample. The tube was then transferred back to the analysis port of the gas adsorption instrument. The outgas rate was again confirmed to be less than 3 μbar min^{-1}. For all isotherms, warm and cold free space correction measurements were performed using ultra-high purity He gas (99.999% purity); N_2 isotherms at 77 K were measured in liquid N_2 baths using UHP-grade gas sources. Oil-free vacuum pumps and oil-free pressure regulators were used for all measurements to prevent contamination of the samples during the evacuation process or of the feed gases during the isotherm measurements. Langmuir and

Brunauer–Emmett–Teller (BET) surface areas were determined from N_2 adsorption data at 77 K using Micromeritics software.

Ethylene oligomerization reactions. In an N_2-filled glovebox, microcrystalline powder of activated material (5–30 mg) was placed in a reactor built from a Swagelok® 10 mL stainless steel sample cylinder and a Swagelok® stainless steel ball valve. Cyclohexane, Et_2AlCl (100 equivalents per Ni or Zr), undecane (internal standard), and a PTFE stir bar were added, ensuring that the total volume was consistently 5.0 mL. The reactor was sealed, removed from the glovebox, weighed, and then attached to a custom-built stainless steel high-pressure manifold kept under dynamic vacuum. Once the headspace was fully evacuated, the manifold was pressurized with 59 bar of ethylene. The sample cylinders were then carefully pressurized by partially opening the ball valves and heated at 55 °C for 1 h with magnetic stirring. At this time, the reactors were immediately sealed and cooled for 20 min in a dry ice/isopropanol bath. With the reactor valve partially opened, the manifold was gradually vented to atmospheric pressure. The reactor was warmed to room temperature with the valve closed to prevent bumping of the reaction mixture into the manifold. After the pressure was carefully relieved, the reactor was sealed, detached from the manifold, and then weighed again to determine the total amount of ethylene consumed. The reaction mixture was then added to 1.0 mL of a 6.8% aqueous HCl solution kept in an ice bath. Once the excess Et_2AlCl was fully quenched, a 1.0 mL aliquot of the cylcohexane layer was withdrawn and filtered through a 0.2 μm PTFE syringe filter, and then analyzed by gas chromatography. Note that, prior to each experiment, the reactors were thoroughly washed with successive ~10 mL aliquots of a 34% aqueous HNO_3 solution and deionized water to remove residual contaminants, which were found to cause background catalytic activity.

Results and discussion

Synthesis and metalation of metal–organic frameworks

The metal–organic framework $Zr_6O_4(OH)_4(bpydc)_6$ (**1**) was prepared by a slight modification to a previously published procedure, and the resulting product was found to display a powder X-ray diffraction pattern and Langmuir surface area (Table 1) consistent with those previously reported.[18] With the intent of synthesizing

Table 1 Nickel loading and surface areas of the metal–organic frameworks investigated in this work

Compound	Ni loading[a] (%)	SA_{Lang}[b] ($m^2\ g^{-1}$)	SA_{BET}[c] ($m^2\ g^{-1}$)
1	—	2743 ± 2, 2772 (ref. 18)	2730 (ref. 18)
2	—	2634 ± 2	2430 ± 20
3	—	2805 (ref. 18)	2625 (ref. 18)
1$(NiBr_2)_6$	101 ± 2	650 ± 8	545 ± 3
2$(NiBr_2)_{0.84}$	14.1 ± 0.2	2467 ± 2	2300 ± 20
3$(NiBr_2)_{0.14}$	2.30 ± 0.06	2450 ± 10	—

[a] Nickel loading was determined by ICP-OES analysis based on the molar ratio of Ni relative to Zr in the framework. [b] SA_{Lang} = Langmuir surface area. [c] SA_{BET} = Brunauer–Emmett–Teller (BET) surface area.

a framework with a lower concentration of uniformly dispersed bipyridine sites relative to **1**, the mixed-linker framework $Zr_6O_4(OH)_4(bpydc)_{0.84}(bpdc)_{5.16}$ (**2**) was synthesized by reacting $ZrCl_4$ with a 1 : 9 mixture of H_2bpydc and H_2bpdc in the presence of benzoic acid, following the same synthetic method developed for **1**. The powder X-ray diffraction data show that **2** is isostructural to **1** (Fig. S3†). Analysis of a sample of **2** digested in a solution of HF and DMSO-d_6 by ^{1}H NMR revealed that 14% of the linkers correspond to $bpydc^{2-}$. Fully-desolvated **2** exhibits Langmuir and BET surface areas of 2630 $m^2\ g^{-1}$ and 2430 $m^2\ g^{-1}$ (Table 1), respectively, which are slightly lower than the reported surface areas of **1**. Thermogravimetric analysis of the thermal decomposition of **2** under flowing N_2 (Fig. S17†) showed that, after desolvation, the framework remains stable at temperatures up to 450 °C, at which point a sharp decrease in mass associated with framework decomposition occurs.

Molecular nickel(II) bipyridine and α-diimine precatalysts studied for ethylene oligomerization are generally synthesized by reaction of the corresponding ligand with Ni(DME)Br_2 in CH_2Cl_2 at room temperature for 18 h.[35,57] Post-synthetic metalation of metal–organic frameworks, however, often requires higher temperatures and longer reaction times to achieve high metal loadings. Thus, DME was selected as a solvent for metalation to allow for higher reaction temperatures without significantly changing the coordination environment of the nickel(II) complexes in the metalated frameworks. In addition, the DME-solvated $NiBr_2$ complexes are sufficiently small to fit through the triangular windows of the frameworks, which have an incircle diameter of ~8 Å. Thus, suspending microcrystalline powders of **1** or **2** with one equivalent of Ni(DME)Br_2 per bipyridine linker at 80 °C for 5 days yielded **1**$(NiBr_2)_6$ and **2**$(NiBr_2)_{0.84}$, respectively, as pale yellow powders. These microcrystalline powders retain their color after three 24 h DME washes, suggesting the successful metalation of the frameworks. Determination of the nickel to zirconium ratios by ICP-OES analysis confirmed the full metalation of the bipyridine sites in both **1** and **2** (Table 1). Low-pressure N_2 adsorption data collected at 77 K for the metalated frameworks show the expected decrease in surface area (Table 1) with increasing nickel loading.

Based on thermogravimetric analysis (Fig. S18 and S19†), **1**$(NiBr_2)_6$ and **2**$(NiBr_2)_{0.84}$ remain intact up to 350 °C and 400 °C, respectively. The lower thermal stability of these frameworks compared to **1** and **2** is consistent with what has been observed for metalated derivatives of **1**.[18] Analysis of the powder X-ray diffraction patterns of **1**$(NiBr_2)_6$ and **2**$(NiBr_2)_{0.84}$ (Fig. S4 and S5†) reveals that both frameworks maintain crystallinity after metalation. The space group of **2** remains $Fm\bar{3}m$ upon metalation to form **2**$(NiBr_2)_{0.84}$ (Table S2 and Fig. S8†). In this space group, crystallographic symmetry imposes disorder of the bipyridine complexes over at least two positions, making their structural characterization exceedingly difficult. Metalation of **1**, however, was found to induce a change in space group from $Fm\bar{3}m$ to the lower-symmetry space group $Pa\bar{3}$ (Table S7 and Fig. S8†), which has been previously reported to be caused by the crystallographic ordering of the metal–bipyridine complexes within the framework.[18]

In contrast to the powder sample, single crystals of **1** treated with the same metalation conditions do not show a change in space group and were found to have a very low nickel loading. This disparity has been previously observed and can be attributed to slow diffusion of the metal source into the crystal interior.[18] To address this problem, higher reaction temperatures were attempted, requiring the replacement of DME with the higher-boiling solvent diglyme. Reaction with

one equivalent of Ni(DME)Br_2 in diglyme at 120 °C for one month results in the single-crystal-to-single-crystal metalation of **1** to form **1**$(NiBr_2)_{5.64}$. Characterization of **1**$(NiBr_2)_{5.64}$ by single-crystal X-ray diffraction revealed that the space group changed to $Pa\bar{3}$, accompanied by ordering of linker–$NiBr_2$ complexes in the framework (Fig. 1). The nickel(II) centers were found to be disordered over two positions tilted 23° apart, with site occupancies of 64% and 30% (Fig. S1†). In addition to the bipyridine linkers, the Br^- ligands could also be resolved but were disordered over several nickel(II) coordination sites. The relative positions and site occupancies of these ligands indicate that 87% of the nickel sites adopt a pseudooctahedral coordination geometry, while the remaining sites appear to be square pyramidal (Fig. S1†). Residual electron density suggests that solvent molecules complete the nickel(II) coordination spheres. These ligands, however, could not be resolved due to disorder and weaker scattering compared to the Br^- ligands. Thus, the nickel coordination geometries cannot be assigned with complete accuracy. These nickel centers likely adopt a tetrahedral geometry, upon desolvation of the framework.

Ethylene oligomerization

In general, ethylene oligomerization reactions were conducted under 59 bar of ethylene at 55 °C for 1 h, which are similar conditions to those reported for molecular nickel(II) bipyridine catalysts.[35] Diethylaluminum chloride was selected as an activating reagent in place of the more commonly used methylaluminoxane (MAO) because it is more likely to fit through the triangular windows of **1** and **2**. Additionally, nickel(II) α-diimine complexes have been found to exhibit comparable activity for ethylene oligomerization with either Et_2AlCl or MAO as activating agents.[34]

The framework **1**$(NiBr_2)_6$ reacts with ethylene to give a range of oligomers (C_4–C_{18+}) in the presence of Et_2AlCl. Surprisingly, C_4–C_{18} oligomers only accounted for 23 ± 1% of the ethylene consumed, while a considerable amount of polymer was recovered from the reaction mixture. Nickel(II) α-diimine catalysts for ethylene polymerization require ligands that enforce steric bulk around positions axial to the square planar active species.[58,59] Blocking these sites inhibits chain termination by preventing the associative substitution of the olefin chain by ethylene (Scheme 1), leading to the formation of polymer instead of oligomers. Bipyridine-based nickel(II) catalysts, however, typically lack the necessary steric bulk to facilitate polymerization,[35,57] suggesting that the formation of polyethylene in **1**$(NiBr_2)_6$ is an effect of the immediate pore environment and not the ligand.

Indeed, further examination of the single-crystal structure of **1** reveals that nearby linker–$NiBr_2$ complexes (within 6 Å) surround the sites above and below each nickel(II) center (Fig. 2). This steric environment coupled with the presence of additional charge-balancing anions can act to impede displacement of the growing alkyl chain, making polymer formation more favorable. In addition, **1**$(NiBr_2)_6$ consumes ethylene at a relatively low average turnover frequency (TOF) of 4300 ± 400 $mol_{ethylene}\ mol_{Ni}^{-1}\ h^{-1}$ (Table 2) under oligomerization conditions. In contrast, molecular nickel(II) bipyridine catalysts selectively produce a Schulz–Flory distribution of oligomers with much higher activities.[35,57] The lower activity of **1**$(NiBr_2)_6$ compared to its molecular analog

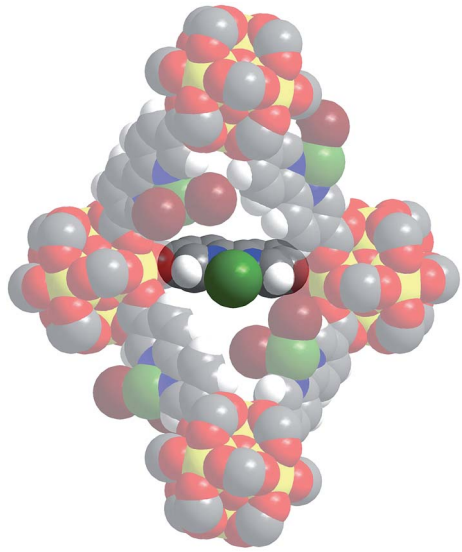

Fig. 2 Space-filling model of a section of the crystal structure of $Zr_6O_4(OH)_4(bpydc)_6(NiBr_2)_{5.64}$ emphasizing the pore environment around the nickel(II)–linker complexes as determined by analysis of single-crystal X-ray diffraction data; yellow, green, dark red, red, blue, and gray spheres represent Zr, Ni, Br, O, N, and C atoms, respectively. The Ni^{II} centers are disordered over two positions (Fig. S1†), but are represented here in only one orientation. Coordinated solvent molecules that complete the Ni^{II} coordination sphere could not be modeled due to disorder and weak scattering compared to the Br^- ligands. Bromine atoms on one of the nickel(II)–linker complexes are omitted for clarity.

$Ni(bpy)Br_2$ (TOF = ~63 000 $mol_{ethylene}$ mol_{Ni}^{-1} h^{-1})[35] likely originates from incomplete activation of the framework nickel(II) complexes by Et_2AlCl. Full metalation of **1** constricts the pore apertures in the framework and decreases its porosity (Table 1), which would in turn hinder diffusion of Et_2AlCl to sites in the crystal interior. This problem is further aggravated upon reaction with Et_2AlCl,

Table 2 Ethylene oligomerization results

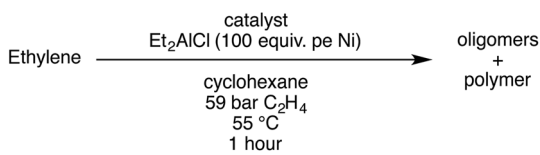

Catalyst	Average TOF[a] ($mol_{ethylene}$ mol_{Ni}^{-1} h^{-1})	Activity[a] ($g_{product}$ $g_{catalyst}^{-1}$ h^{-1})	Weight%[a] (C_{4-18} olefins)
1$(NiBr_2)_6$	4300 ± 400	220 ± 20	23 ± 1
2$(NiBr_2)_{0.84}$	36 000 ± 3000	370 ± 30	73 ± 6
3$(NiBr_2)_{0.14}$	25 000 ± 2000	44 ± 3	91 ± 20

[a] Determined as an average of three replications.

because the proposed cationic nickel active species that forms (Scheme 1) requires a non-coordinating alkyl aluminium halide anion for charge balance.

Initial attempts to relieve the steric congestion around the nickel active sites in **1** by metalation with only 0.1 equivalents Ni(DME)Br_2 gave rise to only a negligible improvement in selectivity for oligomers. Suspecting that surface linker sites were being preferentially metalated, resulting in ineffective dispersion of the nickel active sites, we synthesized the mixed-linker framework **2** to obtain a material with more uniformly dispersed nickel(II)–bipyridine complexes. Gratifyingly, the Ni-metalated framework **2**$(NiBr_2)_{0.84}$ exhibits dramatically increased activity and selectivity for oligomers over polymer (Table 2). Under oligomerization conditions, this material consumes ethylene with an average TOF of 36 000 ± 3000 $mol_{ethylene}$ mol_{Ni}^{-1} h^{-1} and produces 73 ± 6 weight% C_{4-18} oligomers, which approach the activity of the molecular analog.[35,57] Importantly, **2**$(NiBr_2)_{0.84}$ also exhibits higher activity per gram of catalyst compared to **1**$(NiBr_2)_6$, indicating that achieving high metal loadings may not always lead to optimal activity in porous catalysts. The greater activity and selectivity afforded by **2**$(NiBr_2)_{0.84}$ compared to **1**$(NiBr_2)_6$ cannot be attributed to differences in particle size, as SEM images (Fig. S26 and S27†) confirm that both frameworks possess similar particle size distributions (~0.2–2.0 μm). These results demonstrate that active site dilution improves mass transport within the framework and prevents crowding of the active sites, with both effects enabling higher activity and selectivity for oligomers.

To probe for possible pore environment effects on oligomerization selectivity, the product mixtures from these reactions were analyzed for deviations from the expected Schulz–Flory distribution (Fig. 3). In product mixtures that follow this distribution, the ratio of moles produced for oligomers with a chain length of *n*

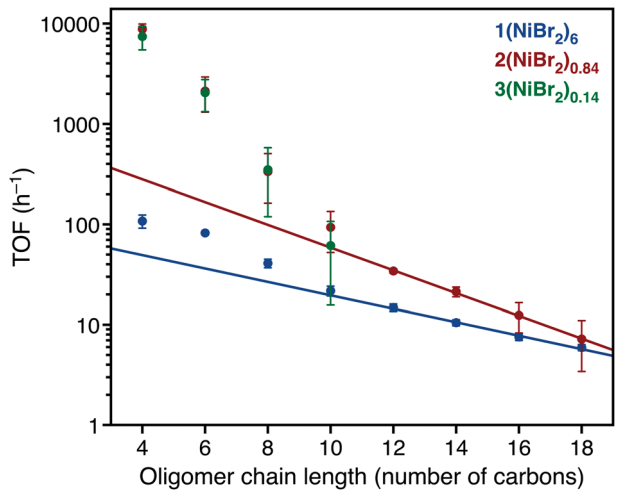

Fig. 3 Average turnover frequency ($mol_{oligomer}$ mol_{Ni}^{-1} h^{-1}) distribution plot for C_{4-18} oligomers produced in ethylene oligomerization reactions catalyzed by **1**$(NiBr_2)_6$ (blue), **2**$(NiBr_2)_{0.84}$ (red), and **3**$(NiBr_2)_{0.14}$ (green). The filled circles represent experimental data and the solid lines represent fits to the data for the C_{12-18} oligomer fractions using the Schulz–Flory equation.

carbons (mol C_n) and that of an oligomer that is one ethylene unit shorter (mol C_{n-2}) is equal to the probability of chain propagation (α) (eqn (1)). This distribution can also be mathematically described using the Schulz–Flory formula (eqn (2); where $\sum$mol C_n is the total molar amount of oligomers), which gives a straight line in the logarithmic plot of mol C_n *versus* chain length n. As a consequence, any deviations from the Schulz–Flory distribution can easily be identified if the product mixture does not follow this linear trend.

$$\frac{\text{mol } C_n}{\text{mol } C_{n-2}} = \alpha = \frac{r_{\text{chain growth}}}{r_{\text{chain growth}} + r_{\text{chain termination}}} \quad (1)$$

$$\text{mol } C_n = (\sum \text{mol } C_n)(1 - \alpha)\alpha^{n-1} \quad (2)$$

To facilitate comparison of the relative activities for each catalyst over the entire range of oligomer chain lengths, eqn (2) can also be expressed in terms of the average turnover frequency for each oligomer chain length (TOF C_n), which is in units of $\text{mol}_{\text{oligomer}}$ per mol_{Ni} per hour (eqn (3)).

$$\text{TOF } C_n = (\sum \text{TOF } C_n)(1 - \alpha)\alpha^{n-1} \quad (3)$$

Remarkably, consistent with the anticipated impact of pore confinement upon oligomerization, both **1**$(NiBr_2)_6$ and **2**$(NiBr_2)_{0.84}$ show enhanced selectivity for shorter oligomers, resulting in deviations from the Schulz–Flory distribution (Fig. 3). Specifically, the C_{12-18} oligomer fractions follow the expected linear trend, while the average turnover frequencies for the C_{4-10} oligomer fractions are higher than expected. From these observations, we reasoned that active sites on the outer surfaces of the crystals might give rise to a Schulz–Flory distribution of oligomers, while sites located in the crystal interior exhibit selectivity for shorter oligomers due to confinement within the pore. In agreement with this hypothesis, a more pronounced deviation was observed for reactions catalyzed by **2**$(NiBr_2)_{0.84}$, in which a greater fraction of nickel sites within the crystal interior are accessible.

Examination of the relative amount of α-olefin in each oligomer fraction (Table S3†) further corroborates that the pore environment influences oligomerization selectivity. The Schulz–Flory (C_{12-18}) region of the oligomer mixture produced by **1**$(NiBr_2)_6$ contains higher fractions of α-olefins (~83–86%) compared to that of its molecular analog (~55%).[35] This higher selectivity for α-olefins suggests stronger inhibition of chain termination from the internal olefin nickel(II) complexes that form upon isomerization compared to that of α-olefin complexes due to the steric environment around the active nickel sites. Instead, the internal olefins isomerize back to form α-olefins that either continue chain growth or undergo chain termination. Conversely, **2**$(NiBr_2)_{0.84}$ displays lower selectivity (~50%) for α-olefins in the C_{12-18} fraction, agreeing with the description of the dispersed linker–nickel(II) complexes in this framework as sites that behave like molecular bipyridine nickel(II) oligomerization catalysts. Both **1**$(NiBr_2)_6$ and **2**$(NiBr_2)_{0.84}$, however, exhibit much lower selectivities for α-olefins in fractions that show significant deviation from the Schulz–Flory distribution. The decreased selectivity for α-olefins is consistent with a higher probability for chain isomerization at sites that predominantly produce short oligomers, which can be attributed to slower

chain growth brought about by active site confinement within the pores of these frameworks.

Recognizing that the observed product distributions could also arise from the presence of more than one nickel active species in the framework, we performed control experiments to determine if the nickel(II)-bipyridine sites were solely responsible for the observed catalytic activity. No conversion of ethylene to either oligomers or polymer was observed using **1**, confirming that the framework zirconium sites are inactive. The biphenyl variant of **1**, $Zr_6O_4(OH)_4(bpdc)_6$ (**3**), was then prepared and subjected to the same metalation conditions, to check for any adventitious Ni species that could be forming at other sites in the framework. Surprisingly, the Ni-treated framework **3**$(NiBr_2)_{0.14}$ was found to contain 2.30 ± 0.06% Ni for each Zr center by ICP-OES (Table 1), even after extensive washing with DME. Additionally, **3**$(NiBr_2)_{0.14}$ selectively oligomerizes ethylene to produce only C_{4-10} oligomers (Table 2) with poor selectivity for α-olefins. This unexpected activity likely originates from active nickel species coordinated to water and hydroxide ligands that occupy vacant linker sites on the zirconium cluster.[60–62] Similar metal binding sites on the zirconium cluster have been previously reported and studied for catalysis in other frameworks.[25,63,64] For instance, the framework NU-1000, which possesses four vacant linker coordination sites on its zirconium clusters, has been shown to be active for ethylene oligomerization upon metalation of these sites with nickel salts.[25]

These control experiments strongly suggest that the observed deviations from the Schulz–Flory distribution in **1**$(NiBr_2)_6$ and **2**$(NiBr_2)_{0.84}$ result in part from the formation of at least two different types of active sites, nickel(II)–bipyridine complexes and nickel species similar to those present in **3**$(NiBr_2)_{0.14}$. Assuming, however, that the same amount of the nickel species in **3**$(NiBr_2)_{0.14}$ also exist in **2**$(NiBr_2)_{0.84}$ (17% of the Ni^{II} sites), activity from these sites would only account for around 16 ± 4% by mass of the oligomers formed in excess of the amounts estimated from the Schulz–Flory distribution (Fig. S20†). Thus, the contribution of pore confinement effects to the selectivity for C_{4-10} oligomers in these frameworks cannot be ruled out entirely, as it may be possible that the nickel(II)–bipyridine complexes in **2**$(NiBr_2)_{0.84}$ produce the rest of the oligomers associated with the deviation. The presence of two active species, however, precludes the rigorous investigation of such effects in these materials.

Conclusions

Metal–organic frameworks extend the degree of synthetic control and structural characterization available to molecular chemistry to the design of porous solids. These capabilities are distinctly advantageous in the development of heterogeneous systems for industrial processes that currently require homogeneous catalysts. Here, porous solid catalysts featuring active sites derived from molecular nickel(II) bipyridine ethylene oligomerization catalysts have been synthesized through the post-synthetic metalation of the metal–organic frameworks $Zr_6O_4(OH)_4(bpydc)_6$ and $Zr_6O_4(OH)_4(bpydc)_{0.84}(bpdc)_{5.16}$ using $Ni(DME)Br_2$. The pore environment in these materials substantially alters the reactivity of the nickel(II) bipyridine active sites. Specifically, Ni^{II}-metalated $Zr_6O_4(OH)_4(bpydc)_6$ produces considerable amounts of polymer, which contrasts with the selectivity of molecular analogs for oligomers. This unexpected reactivity is ascribed to steric

bulk from nearby linker–$NiBr_2$ complexes that block sites axial to the nickel(II) centers, thereby mimicking the steric environment found in molecular nickel(II) α-diimine polymerization catalysts. Relieving the steric congestion around the active sites by dispersing the nickel(II) bipyridine complexes within the mixed-linker framework $Zr_6O_4(OH)_4(bpydc)_{0.84}(bpdc)_{5.16}$, leads to significantly greater activity and higher selectivity for oligomer formation. Furthermore, both Ni^{II}-metalated frameworks exhibit increased selectivity for C_{4-10} oligomers, giving rise to deviations from the expected Schulz–Flory product distribution. The results of key control experiments show, however, that the combined activity of the nickel(II)–bipyridine complexes and adventitious nickel sites partly account for this unusual product distribution. While confinement effects may still contribute to selectivity for shorter oligomers in these frameworks, the presence of two active sites severely complicates the study of such effects. Altogether, these results serve to emphasize that the apparent active site structure does not necessarily solely dictate reactivity in metal–organic frameworks, as well as that the pore environment around these sites can have profound influences on catalytic behavior.

Acknowledgements

The work was supported by the Nanoporous Materials Genome Center, funded by the U.S. Department of Energy, Office of Basic Energy Sciences, Division of Chemical Sciences, Geosciences and Biosciences, under Award DE-FG02-12ER16362. Single-crystal X-ray diffraction experiments were conducted at Beamline 11.3.1 at the Advanced Light Source, which is supported by the Director, Office of Science, Office of Basic Energy Sciences, of the U.S. Department of Energy under Contract No. DE-AC02-05CH11231. We thank the National Science Foundation for providing graduate fellowship support for J. O. We are grateful for the assistance of Kristen A. Colwell with the SEM measurements. We thank Phillip J. Milner, Dianne J. Xiao, David Z. Zee, Jeffrey D. Martell, and Rebecca L. Siegelman for helpful discussions.

Notes and references

1 J. Hagen, *Industrial Catalysis*, Wiley-VCH Verlag GmbH & Co. KGaA, Weinheim, 2006.
2 A. Behr, *Catalysis, Homogeneous. Ullman's Encyclopedia of Industrial Chemistry*, Wiley-VCH, Weinheim, 2012, vol. 7, pp. 223–269.
3 S. Bhaduri and D. Mukesh, *Homogeneous Catalysis: Mechanisms and Industrial Applications*, John Wiley & Sons, Inc., 2000.
4 A. Forestière and H. Olivier-Bourbigou, *Oil Gas Sci. Technol.*, 2009, **64**, 649–667.
5 G. P. Belov and P. E. Matkovsky, *Pet. Chem.*, 2010, **50**, 283–289.
6 P. W. N. M. van Leeuwen, N. D. Clément and M. J. L. Tschan, *Coord. Chem. Rev.*, 2011, **255**, 1499–1517.
7 A. Finiels, F. Fajula and V. Hulea, *Catal. Sci. Technol.*, 2014, **4**, 2412–2415.
8 A. Galletti, G. Geri, G. Sbrana and M. Marchionna, *J. Mol. Catal. A: Chem.*, 1996, **111**, 273–280.
9 G. Braca, A. Galletti, M. Di Girolamo and G. Sbrana, *J. Mol. Catal. A: Chem.*, 1995, **96**, 203–213.

10 H. Toulhoat, M. Lontsi Fomena and T. de Bruin, *J. Am. Chem. Soc.*, 2011, **133**, 2481–2491.
11 W. Keim, *Angew. Chem., Int. Ed.*, 1990, **29**, 235–244.
12 W. Keim, *Angew. Chem., Int. Ed.*, 2013, **52**, 12492–12496.
13 B. L. Small and M. Brookhart, *J. Am. Chem. Soc.*, 1998, **120**, 7143–7144.
14 F. Speiser, P. Braunstein and L. Saussine, *Acc. Chem. Res.*, 2005, **38**, 784–793.
15 D. S. McGuinness, *Chem. Rev.*, 2011, **111**, 2321–2341.
16 T. Agapie, *Coord. Chem. Rev.*, 2011, **255**, 861–880.
17 J. T. Dixon, M. J. Green, F. M. Hess and D. H. Morgan, *J. Organomet. Chem.*, 2004, **689**, 3641–3668.
18 M. I. Gonzalez, E. D. Bloch, J. A. Mason, S. J. Teat and J. R. Long, *Inorg. Chem.*, 2015, **54**, 2995–3005.
19 K. Manna, T. Zhang and W. Lin, *J. Am. Chem. Soc.*, 2014, **136**, 6566–6569.
20 K. Manna, T. Zhang, M. Carboni, C. W. Abney and W. Lin, *J. Am. Chem. Soc.*, 2014, **136**, 13182–13185.
21 K. Manna, T. Zhang, F. X. Greene and W. Lin, *J. Am. Chem. Soc.*, 2015, **137**, 2665–2673.
22 H. Fei and S. M. Cohen, *Chem. Commun.*, 2014, **50**, 4810–4812.
23 D. J. Xiao, E. D. Bloch, J. A. Mason, W. L. Queen, M. R. Hudson, N. Planas, J. Borycz, A. L. Dzubak, P. Verma, K. Lee, F. Bonino, V. Crocellà, J. Yano, S. Bordiga, D. G. Truhlar, L. Gagliardi, C. M. Brown and J. R. Long, *Nat. Chem.*, 2014, **6**, 590–595.
24 T. Zhang, K. Manna and W. Lin, *J. Am. Chem. Soc.*, 2016, **138**, 3241–3249.
25 Z. Li, N. M. Schweitzer, A. B. League, V. Bernales, A. W. Peters, A. B. Getsoian, T. C. Wang, J. T. Miller, A. Vjunov, J. L. Fulton, J. A. Lercher, C. J. Cramer, L. Gagliardi, J. T. Hupp and O. K. Farha, *J. Am. Chem. Soc.*, 2016, **138**, 1977–1982.
26 E. D. Metzger, C. K. Brozek, R. J. Comito and M. Dincă, *ACS Cent. Sci.*, 2016, **2**, 148–153.
27 E. D. Metzger, R. J. Comito, C. H. Hendon and M. Dincă, *J. Am. Chem. Soc.*, 2017, **139**, 757–762.
28 J. Canivet, S. Aguado, Y. Schuurman and D. Farrusseng, *J. Am. Chem. Soc.*, 2013, **135**, 4195–4198.
29 S. T. Madrahimov, J. R. Gallagher, G. Zhang, Z. Meinhart, S. J. Garibay, M. Delferro, J. T. Miller, O. K. Farha, J. T. Hupp and S. T. Nguyen, *ACS Catal.*, 2015, **5**, 6713–6718.
30 B. Liu, S. Jie, Z. Bu and B.-G. Li, *RSC Adv.*, 2014, **4**, 62343–62346.
31 S. Liu, Y. Zhang, Y. Han, G. Feng, F. Gao and H. Wang, *Organometallics*, 2017, **36**, 632–638.
32 A. N. Mlinar, B. K. Keitz, D. Gygi, E. D. Bloch, J. R. Long and A. T. Bell, *ACS Catal.*, 2014, **4**, 717–721.
33 G. J. P. Britovsek, R. Malinowski, D. S. McGuinness, J. D. Nobbs, A. K. Tomov, A. W. Wadsley and C. T. Young, *ACS Catal.*, 2015, **5**, 6922–6925.
34 S. A. Svejda and M. Brookhart, *Organometallics*, 1999, **18**, 65–74.
35 C. M. Killian, L. K. Johnson and M. Brookhart, *Organometallics*, 1997, **16**, 2005–2007.
36 D. J. Xiao, J. Oktawiec, P. J. Milner and J. R. Long, *J. Am. Chem. Soc.*, 2016, **138**, 14371–14379.

37 C. Kutzscher, G. Nickerl, I. Senkovska and V. Bon, *Chem. Mater.*, 2016, **28**, 2573–2580.
38 J. D. Evans, C. J. Sumby and C. J. Doonan, *Chem. Soc. Rev.*, 2014, **43**, 5933–5951.
39 S. M. Cohen, Z. Zhang and J. A. Boissonnault, *Inorg. Chem.*, 2016, **55**, 7281–7290.
40 P. V. Dau and S. M. Cohen, *Chem. Commun.*, 2013, **49**, 6128–6130.
41 T.-J. J. Kinnunen, M. Haukka, T. T. Pakkanen and T. A. Pakkanen, *J. Organomet. Chem.*, 2000, **613**, 257–262.
42 M. Helldörfer, W. Milius and H. G. Alt, *J. Mol. Catal. A: Chem.*, 2003, **197**, 1–13.
43 L. Li, S. Tang, C. Wang, X. Lv, M. Jiang, H. Wu and X. Zhao, *Chem. Commun.*, 2014, **50**, 2304–2307.
44 J. H. Cavka, S. Jakobsen, U. Olsbye, N. Guillou, C. Lamberti, S. Bordiga and K. P. Lillerud, *J. Am. Chem. Soc.*, 2008, **130**, 13850–13851.
45 H. Fei, M. D. Sampson, Y. Lee, C. P. Kubiak and S. M. Cohen, *Inorg. Chem.*, 2015, **54**, 6821–6828.
46 G. Rama, A. Ardá, J.-D. Maréchal, I. Gamba, H. Ishida, J. Jiménez-Barbero, M. E. Vázquez and M. Vázquez López, *Chem.–Eur. J.*, 2012, **18**, 7030–7035.
47 Bruker Analytical X-ray Systems, Inc., *SAINT and APEX 2 Software for CCD Diffractometers*, Bruker Analytical X-ray Systems, Inc., Madison, WI, USA, 2000.
48 G. M. Sheldrick, *SADABS*, Bruker Analytical X-ray Systems, Inc., Madison, WI, USA, 2014.
49 G. M. Sheldrick, *SHELXS*, University of Göttingen, Germany, 2014.
50 G. M. Sheldrick, *Acta Crystallogr., Sect. A: Found. Crystallogr.*, 2008, **64**, 112–122.
51 G. M. Sheldrick, *SHELXL*, University of Göttingen, Germany, 2014.
52 O. V. Dolomanov, L. J. Bourhis, R. J. Gildea, J. A. K. Howard and H. Puschmann, *J. Appl. Crystallogr.*, 2009, **42**, 339–341.
53 A. L. Spek, *Acta Crystallogr., Sect. C: Struct. Chem.*, 2015, **71**, 9–18.
54 A. L. Spek, *J. Appl. Crystallogr.*, 2003, **36**, 7–13.
55 A. A. Coelho, *J. Appl. Crystallogr.*, 2003, **36**, 86–95.
56 A. A. Coelho, *TOPAS-Academic, Version 4.1*, Coelho Software, Brisbane, 2007.
57 T. Kinnunen, M. Haukka and T. T. Pakkanen, *J. Organomet. Chem.*, 2000, **613**, 257–262.
58 L. K. Johnson, C. M. Killian and M. Brookhart, *J. Am. Chem. Soc.*, 1995, **117**, 6414–6415.
59 S. D. Ittel, L. K. Johnson and M. Brookhart, *Chem. Rev.*, 2000, **100**, 1169–1204.
60 G. C. Shearer, S. Chavan, S. Bordiga, S. Svelle, U. Olsbye and K. P. Lillerud, *Chem. Mater.*, 2016, **28**, 3749–3761.
61 C. A. Trickett, K. J. Gagnon, S. Lee, F. Gándara, H.-B. Buergi and O. M. Yaghi, *Angew. Chem., Int. Ed.*, 2015, **54**, 11162–11167.
62 G. C. Shearer, S. Chavan, J. Ethiraj, J. G. Vitillo, S. Svelle, U. Olsbye, C. Lamberti, S. Bordiga and K. P. Lillerud, *Chem. Mater.*, 2014, **26**, 4068–4071.
63 K. Manna, P. Ji, F. X. Greene and W. Lin, *J. Am. Chem. Soc.*, 2016, **138**, 7488–7491.
64 S. Yuan, Y.-P. Chen, J. Qin, W. Lu, X. Wang, Q. Zhang, M. Bosch, T.-F. Liu, X. Lian and H.-C. Zhou, *Angew. Chem.*, 2015, **127**, 14909–14913.